Estimating process noise variance of PPP-RTK corrections
a means for sensing the ionospheric time-variability

Sadegh Nojehdeh, Parvaneh; Khodabandeh, Amir; Khoshelham, Kourosh; Amiri-Simkooei, Alireza

DOI
10.1007/s10291-023-01577-4

Publication date
2023

Document Version
Final published version

Published in
GPS Solutions

Citation (APA)
Sadegh Nojehdeh, P., Khodabandeh, A., Khoshelham, K., & Amiri-Simkooei, A. (2023). Estimating process noise variance of PPP-RTK corrections: a means for sensing the ionospheric time-variability. *GPS Solutions*, *28*(1), Article 43. https://doi.org/10.1007/s10291-023-01577-4

GPS Solutions (2024) 28:43
https://doi.org/10.1007/s10291-023-01577-4

ORIGINAL ARTICLE

Estimating process noise variance of PPP-RTK corrections: a means for sensing the ionospheric time-variability

Parvaneh Sadegh Nojehdeh[1] · Amir Khodabandeh[1] · Kourosh Khoshelham[1] · Alireza Amiri-Simkooei[2]

Received: 24 July 2023 / Accepted: 6 November 2023

Abstract
The provision of accurate ionospheric corrections in PPP-RTK enormously improves the performance of single-receiver user integer ambiguity resolution (IAR), thus enabling fast high precision positioning. While an external provider can disseminate such corrections to the user with a time delay, it is the task of the user to accurately time-predict the corrections so that they become applicable to the user positioning time. Accurate time prediction of the corrections requires a dynamic model in which the process noise of the corrections has to be correctly specified. In this contribution, we present an estimation method to determine the process noise variance of PPP-RTK corrections using single-receiver GNSS data. Our focus is on variance estimation of the first-order slant ionospheric delays, which allows one to analyze how the ionospheric process noise changes as a function of the solar activity, receiver local time, and receiver geographic latitude. By analyzing 11-year GNSS datasets, it is illustrated that estimates of the ionospheric process noise are strongly correlated with the solar flux index F10.7. These estimates also indicate a seasonal variation, with the highest level of variation observed during the spring and autumn equinoxes.

Keywords Ionospheric time-variability · Process noise variance-estimation · Precise point positioning-real-time kinematic (PPP-RTK) · Correction latency

Introduction

The provision of accurate ionospheric parameter solutions enormously improves the performance of single-receiver integer ambiguity resolution (IAR) on which the concept of precise point positioning-real-time kinematic (PPP-RTK) is founded (Collins et al. 2012; Odijk et al. 2016; Zha et al. 2021). As with the other types of state-space representation (SSR) corrections, e.g., satellite orbit and clock products, the ionospheric solutions may be provided to the PPP-RTK user with a time delay or latency so as to reduce the transmission rate of the corrections (Wübbena et al. 2005). Each correction type can have its own transmission rate depending on its temporal behavior. For instance, phase-bias corrections do not need a high transmission rate as they are rather stable over time (Zhang et al. 2017). On the other hand, clock and ionospheric corrections demand high transmission rates due to their time-varying nature.

The reception of time-delayed corrections implies that the user has to bridge the time gap between the time the corrections are generated and the time the user applies them to his GNSS data (Wang et al. 2017). The user makes use of the dynamic model of the corrections that is employed by the Kalman filter of the PPP-RTK provider so as to time-predict the corrections (Khodabandeh 2021). The quality with which such prediction is made depends on three main factors: (1) the precision of the corrections generated by the provider, (2) the correction latency, and (3) the validity of the dynamic model of the corrections (Psychas et al. 2022). The necessity of the first factor is rather straightforward. The more precise the corrections, the more precise their time-predicted versions become. Likewise, the role of the second factor, i.e., the correction latency, follows from the fact that the prediction quality deteriorates as the time-delay increases. The third factor states that one must correctly specify the temporal behavior of the corrections. Otherwise, the presence of any

✉ Parvaneh Sadegh Nojehdeh
psadeghnojeh@student.unimelb.edu.au

[1] Department of Infrastructure Engineering, The University of Melbourne, Melbourne, Australia

[2] Department of Geoscience and Remote Sensing, Delft University of Technology, 2600 AA Delft, The Netherlands

misspecification in the dynamic model may lead to large prediction errors. Despite the importance of the third factor, little attention has so far been paid to the estimation of the dynamic model of the corrections. The topic of the present contribution concerns the third factor where we aim to address how the process noise of the corrections, involved in their dynamic model, can be reliably specified using GNSS data. Particular attention will be given to the variance-estimation of the first-order slant ionospheric delays, showing how it measures the ionospheric time-variability as a function of the solar activity and seasonal variations, local time, and the geographic latitude of the receiver (Araujo-Pradere et al. 2005; Hernández-Pajares et al. 2011).

As shown by Psychas et al. (2022), the presence of prediction errors of the corrections should be carefully incorporated into the user parameter estimation method. Otherwise, the user ambiguity success rate would considerably decrease when experiencing high correction latencies, deteriorating the user ambiguity-resolved positioning performance. Furthermore, ignoring such prediction errors may cause the user estimation method to fail to correctly report the precision description of the parameter solutions. They also proposed a scheme for weighting corrected data of the user to account for the uncertainty of the time-predicted corrections. The scheme does, however, rely on the assumption that the variances of the process noises of the corrections are correctly specified. In practice, these variances are often set to take nominal values. One can, however, directly determine these variances using real-world GNSS data. In this contribution, we present a simple estimation method for the determination of the process noise variance of PPP-RTK corrections via a single GNSS receiver. The proposed method is based on the principle of least-squares variance component estimation (Amiri-Simkooei 2007; Teunissen and Amiri-Simkooei 2008). Next to providing insights into the time-variability of the slant ionospheric delays, we analyze 11-year GNSS datasets to illustrate how the estimated variance of the ionospheric process noise is driven by the solar flux index F10.7 (King and Papitashvili 2005).

To show how the time prediction of the corrections governs the user IAR performance, we first conduct a model-driven analysis. It is thereby addressed why one should correctly specify process noise of the corrections to avoid reporting incorrect precision description of the user parameter solutions, bypassing a potential reduction in the user ambiguity success rate. Afterward, we present a process noise variance-estimation method by formulating a system of observation equations, containing known combinations of single-receiver GNSS data. To show the performance of the proposed method at work, we will analyze datasets of several globally distributed GNSS permanent stations. It is shown how the estimated variances of the process noise of the corrections respond to various contributing factors, ranging from the solar activity to the quality of satellite orbit products.

User ambiguity resolution driven by the process noise of the corrections

In this section, we review how the time-variability of PPP-RTK corrections takes a prominent role in governing the user IAR performance. The uncertainty involved in such time-variability shall be captured by the variance matrix of the user corrected observations (Psychas et al. 2022). How such variance matrix should be specified is discussed, and the consequences of misspecifying this matrix are highlighted via an example of single-station PPP-RTK.

How to weight corrected observations of the user

We commence with the single-receiver PPP-RTK user observation equations in their linearized form at epoch i

$$y_i = A_i x_i + C_i c_i + n_i \tag{1}$$

where the user observation vector y_i, together with the measurement noise n_i, is linked to the user-specific unknown parameter vector x_i through the full-rank design matrix A_i. Likewise, the full-rank design matrix C_i links the observations to vector c_i containing the unknown corrections. The observation vector y_i contains GNSS carrier-phase and code measurements, while x_i may contain the user position coordinates, carrier-phase ambiguities, receiver clock offsets with instrumental biases. The correction vector c_i contains estimable forms of satellite orbit and clock parameters, atmospheric delays, and satellite biases (Leick et al. 2015). Although both the design matrices A_i and C_i are of full-column rank, their augmented version $[A_i, C_i]$ is rank-deficient, meaning that the user cannot jointly determine both the unknown vectors x_i and c_i with the sole use of his measurements (Odijk et al. 2016). That is why the user relies on a provider, e.g., a network of permanent GNSS stations (Wübbena et al. 2005), to receive a solution of the correction vector c_i.

To deliver a solution of c_i, the PPP-RTK provider often formulates a Kalman filter to recursively process GNSS data over time. The provision of such a solution is subject to time delay, though. This is because the provider aims to reduce the transmission rate of the corrections (Wübbena et al. 2005). Consequently, the user must time-predict the corrections using the solution that is provided with latency. Although each individual correction type (e.g., clocks or phase biases) has its own latency, in the following, all correction types are assumed to have only one common latency

τ for the sake of presentation. With vector $\hat{c}_{i-\tau}$ denoting the solution of such delayed corrections, the user can bridge the latency τ with the aid of the dynamic model of corrections underlying the Kalman filter of the provider. Accordingly, the solution of c_i is time-predicted as follows (Wang et al. 2017)

$$\hat{c}_{i|i-\tau} = \Phi_{i,i-\tau}\hat{c}_{i-\tau} \quad \text{with} \quad Q^c_{i|i-\tau} = \Phi_{i,i-\tau}Q^c_{i-\tau}\Phi^T_{i,i-\tau} + S_{i,i-\tau} \tag{2}$$

where $\hat{c}_{i|i-\tau}$ denotes the predicted corrections. The transition matrix $\Phi_{i,i-\tau}$ links the corrections from epoch $(i-\tau)$ to epoch i. The variance matrix of $\hat{c}_{i|i-\tau}$ is denoted by $Q^c_{i|i-\tau}$. Likewise, $Q^c_{i-\tau}$ denotes the variance matrix of $\hat{c}_{i-\tau}$. The additional variance matrix $S_{i,i-\tau}$ indicates the increase in the uncertainty of the corrections. This matrix is formed by the process noise of the corrections. If the variance matrix of the process noise of the corrections is given by matrix S, the variance matrix $S_{i,i-\tau}$ can be shown to read (Khodabandeh et al. 2023)

$$S_{i,i-\tau} = \sum_{j=i-\tau+1}^{i} \Phi_{i,j}S\Phi^T_{i,j} \quad \text{with} \quad S_{i,i} = 0 \tag{3}$$

The special case $S_{i,i-\tau} = S_{i,i}$ occurs when $\tau = 0$, that is, when the corrections are sent to the user without any time delay. Given the time-predicted corrections $\hat{c}_{i|i-\tau}$, the user makes the system of Eqs. (1) solvable as

$$\tilde{y}_i = A_i x_i + e_i \quad \text{with} \quad \tilde{y}_i = y_i - C_i\hat{c}_{i|i-\tau} \tag{4}$$

and the residual vector $e_i = C_i\left(c_i - \hat{c}_{i|i-\tau}\right) + n_i$. Therefore, the corrected observations $\tilde{y}_i$ replace the original observations y_i. This, in turn, implies that the user should take the variance matrix of $\tilde{y}_i$, instead that of y_i, for the weighting of the corrected observations. An application of the variance propagation law to $\tilde{y}_i$ gives its variance matrix $Q_{\tilde{y}_i}$ as

$$Q_{\tilde{y}_i} = Q_{y_i} + C_i Q^c_{i|i-\tau} C^T_i \tag{5}$$

where Q_{y_i} denotes the variance matrix of y_i. Thus, the variance matrix $Q_{\tilde{y}_i}$ captures the uncertainty involved in both the original observation vector y_i and the corrections $\hat{c}_{i|i-\tau}$. The user needs to employ the weight matrix $W = Q^{-1}_{\tilde{y}_i}$, i.e., the inverse of the variance matrix of the corrected observations, to achieve minimum-variance least-squares parameter solutions.

Consequences of a misspecified weight matrix

In practice, the variance matrix of the corrections $Q^c_{i|i-\tau}$, given in (2) is not provided to the user. Psychas et al. (2022) showed that this matrix can be well approximated by the variance matrix $S_{i,i-\tau}$ provided that the initialization duration of the Kalman filter of the provider becomes sufficiently long (e.g., about 1 h) so that the approximation $Q^c_{i-\tau} \approx 0$ remains valid. Under this condition, the user may adopt one of the following three cases to form the weight matrix

$$W = \begin{cases} Q^{-1}_{y_i} & \text{Case1} \\ \left(Q_{y_i} + C_i\bar{S}_{i,i-\tau}C^T_i\right)^{-1} & \text{Case2} \\ \left(Q_{y_i} + C_iS_{i,i-\tau}C^T_i\right)^{-1} & \text{Case3} \end{cases} \tag{6}$$

Case 1 concerns the situation in which the user ignores the uncertainty of the corrections. Case 2 accounts for the correctional uncertainty. However, Case 2 relies on an approximate version of $S_{i,i-\tau}$, indicated by $\bar{S}_{i,i-\tau}$, that is formed by nominal values of the process noise variances. Case 3 uses the true values (5) of the process noise variances to structure the variance matrix $S_{i,i-\tau}$. Thus, Case 3 delivers close-to-optimal (minimum-variance) solutions. With reference to the second expression of (3), the weight matrix W would take its simplest form, i.e., $W = Q^{-1}_{y_i}$, for all the three cases if there is no correction latency ($\tau = 0$). This follows by substituting $\bar{S}_{i,i} = S_{i,i} = 0$ into (6). Therefore, the difference between the performances of these three cases is felt only when the corrections arrive with a nonzero latency $\tau > 0$.

With the approximation $Q^c_{i|i-\tau} \approx S_{i,i-\tau}$, Case 3 indicates the optimal choice of the weight matrix W, whereas Cases 1 and 2 are viewed as its misspecified versions. To appreciate the consequences of choosing the weight matrices (6), let us consider a GNSS setup in which a user (station PERT) receives corrections from a provider (station CUT0). Both stations PERT and CUT0 are in Perth, Western Australia (about 20 km apart). An overview of the GNSS dataset and parameter configurations is presented in Table 1. We adopt the dynamic model utilized by Psychas et al. (2022) to model the time behavior of the corrections. The satellite biases are assumed time-constant, the ionospheric delays follow a constant-state process, while the satellite clocks follow a constant-velocity process. However, the standard deviations (STDs) of their nominal and the true process noises are assumed to be different. The variance matrix $\bar{S}_{i,i-\tau}$, in (6), is thus different from its true counterpart $S_{i,i-\tau}$. In the next section, we address why such assumptions are made.

Minimum-variance solutions may not be achieved upon using a misspecified weight matrix. However, losing such optimality property is not the sole consequence. Another consequence is that the inverse of the corresponding least-square normal matrix does not represent the true variance matrix of the solutions (Teunissen 2000). Figure 1 shows the STDs of the positioning solutions before performing IAR, i.e., the ambiguity-float solutions. The true STD values (solid lines) start deviating from their reported versions (dashed lines) when latency of the corrections

Table 1 GNSS dataset and parameter configurations concerning the weight matrices (6). The letter z denotes the zenith angle [deg] of the ionospheric piercing point of each satellite

GNSS data	
Provider station	CUT0
User station	PERT
Phase and code data	GPS (L1/L2), Galileo (E1/E5a)
Date	1st of September 2020
Epoch time	02:00 GPS time (single epoch)
Measurement sampling frequency	1 Hz
Stochastic model	
Phase zenith-referenced standard deviation	1.0 mm
Code zenith-referenced standard deviation	20 cm
Elevation weighting	Sine function
Elevation cut-off	10°
Dynamic model	
Phase ambiguities	Time-constant
Satellite biases	Time-constant
Nominal [true] satellite clock process noise	3.0[7.0] mm/$\sqrt{\text{s}}$
Nominal [true] ionospheric process noise	$1.0\left[0.4\exp\left(\frac{z}{15^\circ}\right)\right]$mm/$\sqrt{\text{s}}$
Ambiguity resolution	
Estimation principle	Integer least squares (ILS)
IAR method	Full IAR with LAMBDA

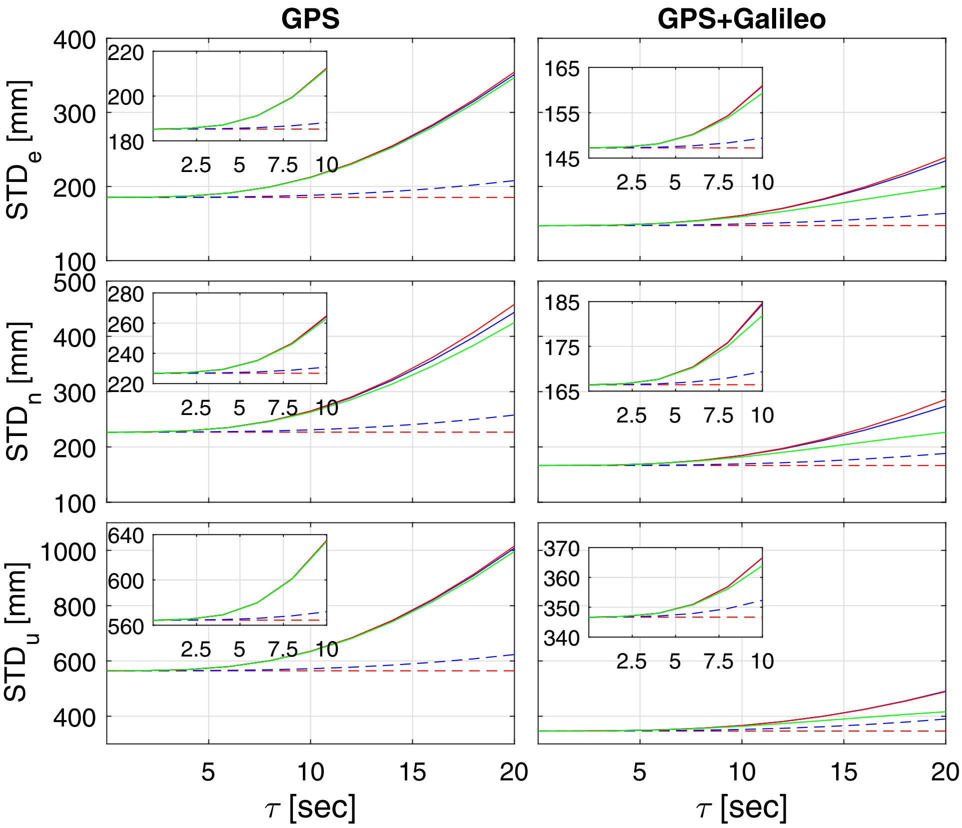

Fig. 1 STDs of the user **ambiguity-float**, single-epoch positioning solutions for East (top), North (middle), and Up (bottom) components using GPS (left) and GPS-plus-Galileo (right) as functions of latency τ. The colors red, blue, and green correspond to Cases 1, 2 and 3 in (6), respectively. The solid lines indicate true values, while the dashed lines indicate reported values

exceeds 5 s. An increase in the number of satellites (e.g., from GPS to GPS-plus-Galileo) can limit such deviations. However, the stated deviations amplify, the longer the latency τ becomes irrespective of the number of involved satellites. The comparison of the true STD values, obtained by Cases 1 to 3, reveals that the solutions do not experience a considerable precision loss though, even for the latencies as long as $\tau = 20$ seconds. Therefore, using the misspecified weight matrices of Cases 1 and 2 does not considerably degrade the precision of the ambiguity-float positioning solutions.

Let us now consider the ambiguity-fixed positioning results. As shown in Fig. 2, not only do the reported STDs deviate from their true counterparts, but also the true STD values, corresponding to Cases 1 and 2, deviate from their optimal versions (Case 3) for latencies longer than $\tau = 5$ seconds. When it comes to IAR, it is thus crucial to properly specify the weight matrix W. We further evaluate and present the user ambiguity success rate as a function of latency τ in Fig. 3. Cases 1 and 2 unrealistically report high ambiguity success rates (dashed lines) even for the correction latencies around $\tau = 20$ seconds. This is because Case 1 ignores the correctional uncertainty, while Case 2 takes a nominal clock process noise (3 mm/$\sqrt{\mathrm{s}}$) that is smaller than its true version (7 mm/$\sqrt{\mathrm{s}}$). Under the GPS-plus-Galileo setup, Case 3 maintains ambiguity success rates larger than 99.8% for a long latency of $\tau = 10$ seconds. However, the corresponding success rate of Case 2 drops to 99.0%. This indicates why it is important to specify the STDs of the process noises for realizing successful IAR.

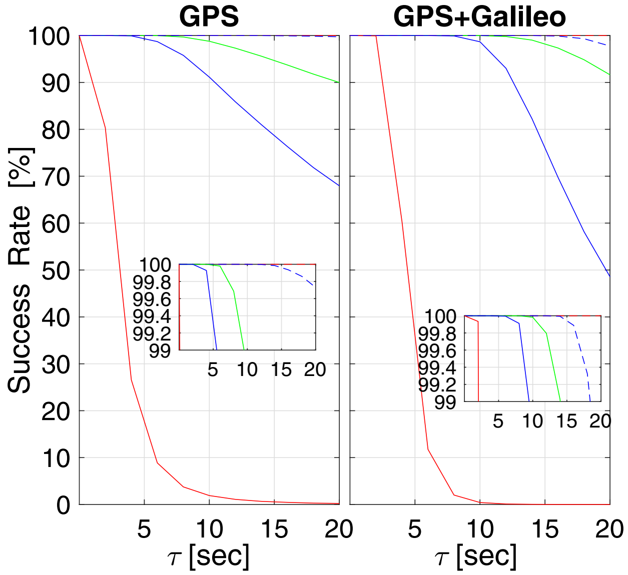

Fig. 3 User single-epoch ambiguity success rates of GPS (left) and GPS-plus-Galileo (right) as a function of latency τ for Cases 1 (red), 2 (blue), and 3 (green), see Fig. 2

Fig. 2 STDs of the user **ambiguity-fixed**, single-epoch positioning solutions for East (top), North (middle), and Up (bottom) components using GPS (left) and GPS-plus-Galileo (right) as functions of latency τ. The colors red, blue, and green correspond to Cases 1, 2 and 3 in (6), respectively. The solid lines indicate true values, while the dashed lines indicate reported values

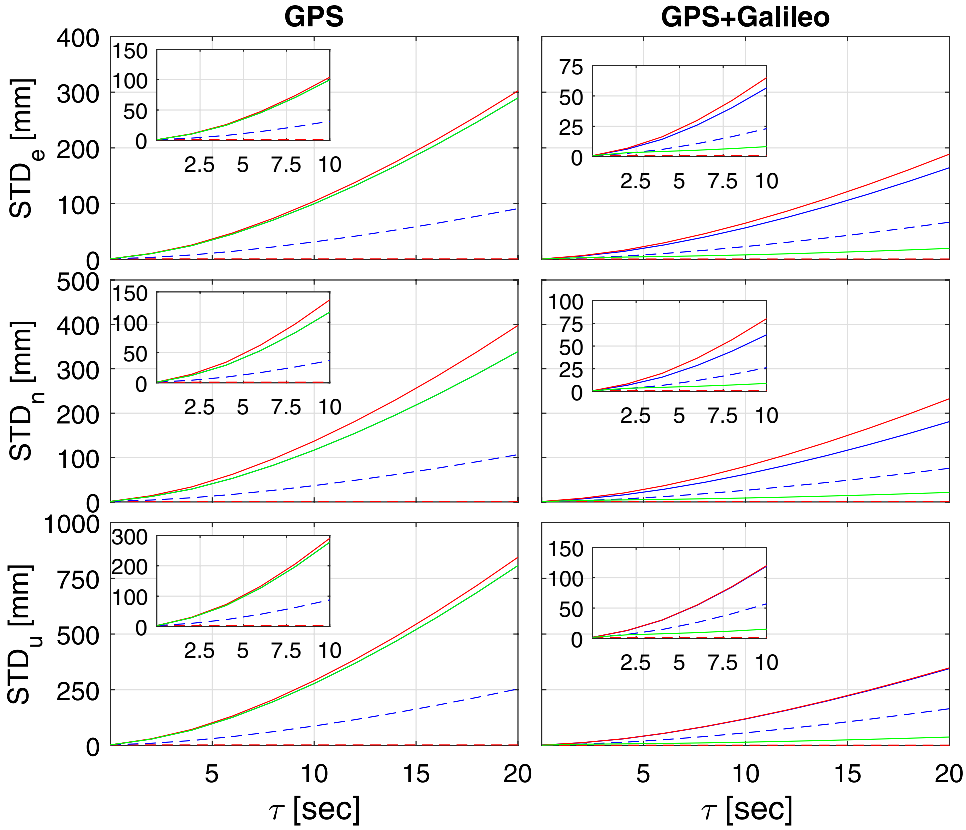

Single-receiver variance estimation of the process noise

So far, the importance of correctly specifying the process noises of the corrections in PPP-RTK user positioning has been discussed. However, how one can infer such noises from GNSS data has not yet been addressed. In this section, we therefore present a simple estimation method to determine the variance of such process noises via a single-receiver GNSS setup. The framework on which the proposed estimation is based is the principle of least-squares variance component estimation (Amiri-Simkooei 2007; Teunissen and Amiri-Simkooei 2008).

Observation equations of the unknown variances

Although a network of GNSS stations often takes the role of the PPP-RTK provider, here, we assume that a single station takes this role. Its system of observation equations resembles that of the user (1), with a difference that here, the parameter vector x_i contains either a-priori known elements (e.g., pre-determined ground-truth position coordinates) or S-basis (datum) parameters (Odijk et al. 2016). Thus, the observation equations of the single-receiver provider follow from (1) by moving the term $A_i x_i$ to the left-hand side of the equations, that is

$$y_i - A_i x_i = C_i c_i + n_i \tag{7}$$

The provider incorporates the above measurement model into his filter to recursively estimate the unknown corrections c_i. How such recursive estimation shall be conducted was previously discussed in Khodabandeh (2021). We now show that the provider can take this one step further and also estimate the variances of the process noise of the corrections c_i. To this end, suppose that the temporal behavior of the corrections is described by the following dynamic model

$$c_i = \Phi_{i,i-1} c_{i-1} + d_i, \quad i = 2, 3, \ldots \tag{8}$$

where the unknown vector d_i contains the zero-mean process noises of the corrections. Compare the above model with (2). It is the dynamic model (8) that allows the user to time-predict the corrections $\hat{c}_{i|i-\tau}$, while it is the variance matrix of d_i (i.e., S in 3), and the latency τ that drives the quality of the prediction. The task is to estimate the entries of S using measurements of the provider $(y_i - A_i x_i)$ in (7). We first determine single-epoch solutions of the corrections, say $\hat{c}_i$, as follows

$$\hat{c}_i = C_i^+ \left(y_i - A_i x_i\right), \quad i = 1, 2, \ldots \tag{9}$$

in which C_i^+ is the least-squares inverse of matrix C_i (Teunissen 2000), i.e., $C_i^+ C_i = I$ (identity matrix). Substitution of the equalities $c_i = \hat{c}_i - C_i^+ n_i$ and $c_{i-1} = \hat{c}_{i-1} - C_{i-1}^+ n_{i-1}$ into $d_i = c_i - \Phi_{i,i-1} c_{i-1}$ gives

$$w_i = d_i + C_i^+ n_i - \Phi_{i,i-1} C_{i-1}^+ n_{i-1}, \quad i = 2, 3, \ldots \tag{10}$$

where the pseudo-observation vector w_i is given by $w_i = \hat{c}_i - \Phi_{i,i-1} \hat{c}_{i-1}$. If no mismodeled effect, such as phase cycle-slip or code multipath, is present, the pseudo-observation vector w_i would then represent a zero-mean random vector. Assuming that the measurement noises n_{i-1} and n_i are mutually uncorrelated with the process noise d_i, the variance matrix of w_i, denoted by Q_{w_i}, follows by applying the variance propagation law. This variance matrix reads

$$Q_{w_i} = S + C_i^+ Q_{n_i} C_i^{+T} + \Phi_{i,i-1} C_{i-1}^+ Q_{n_{i-1}} C_{i-1}^{+T} \Phi_{i,i-1}^T \tag{11}$$

where $Q_{n_{i-1}}$ and Q_{n_i} are the variance matrices of the measurement noises n_{i-1} and n_i, respectively. On the other hand, the definition $E(w_i w_i^T) = Q_{w_i}$ (with symbol E being the expectation operator) implies that the observable matrix $w_i w_i^T$ can serve to estimate the entries of Q_{w_i}. Accordingly, the entries of the process noise variance matrix S can be estimated from the following system of observation equations

$$E(w_i w_i^T) - C_i^+ Q_{n_i} C_i^{+T} - \Phi_{i,i-1} C_{i-1}^+ Q_{n_{i-1}} C_{i-1}^{+T} \Phi_{i,i-1}^T = S \tag{12}$$

The above system of observation equations forms the basis for estimating the unknown entries of matrix S. However, this system relies on having the GNSS measurement variance matrices $Q_{n_{i-1}}$ and Q_{n_i} a-priori known. These matrices contain the satellite elevation-dependent variances of the carrier-phase and code observations. Fortunately, such variance matrices can be a-priori determined via GNSS zero- and short-baseline setups (Amiri-Simkooei and Tiberius 2007). In the following, we assume that these variance matrices are known and given.

Constant-state and -velocity dynamic models

According to (12), one can estimate the entries of S by evaluating the symmetric matrix $w_i w_i^T - C_i^+ Q_{n_i} C_i^{+T} - \Phi_{i,i-1} C_{i-1}^+ Q_{n_{i-1}} C_{i-1}^{+T} \Phi_{i,i-1}^T$ at every epoch $i (i = 2, 3, \ldots)$. Depending on the structure of S, these single-epoch solutions can then be combined in a least-squares sense to deliver the sought-for process noise variance solutions (Amiri-Simkooei 2007). The structure of S is shaped upon adopting a dynamic model for the corrections. We assume that the phase and code biases are constant in time; an assumption that often holds over short time-intervals (Zhang et al. 2017). When the slant ionospheric delays play the role of the corrections c_i, the underlying dynamic model is assumed given by the following constant-state random process

$$\Phi_{i,i-1} = I_m (\text{identity matrix}),$$
$$S = \sigma^2_{\text{iono}} \Delta_t \text{diag}\left(\exp\left(\frac{z_1}{15^\circ}\right), \exp\left(\frac{z_2}{15^\circ}\right), \dots, \exp\left(\frac{z_m}{15^\circ}\right)\right) \tag{13}$$

where Δ_t denotes the measurement sampling-rate, and z_j denotes zenith angle of the ionospheric piercing point for satellite $j(j = 1, \dots, m)$, with m being the number of visible satellites. As a result of this assumption, the $m \times m$ diagonal matrix S contains the ionospheric process noise variance σ^2_{iono} as unknown.

When the satellite clock offsets and their drifts play the role of the corrections c_i, the underlying dynamic model is assumed given by the following constant-velocity random process (Wang et al. 2017)

$$\Phi_{i,i-1} = \begin{bmatrix} I_m & \Delta_t I_m \\ 0 & I_m \end{bmatrix}, \quad S = \sigma^2_{\text{clk}} \begin{bmatrix} \frac{\Delta_t}{2} I_m & 0 \\ 0 & \frac{1}{2\Delta_t} I_m \end{bmatrix} \tag{14}$$

Like the ionospheric dynamic model (13), the 2 m × 2 m diagonal matrix S, in (14), only contains the clock process noise variance σ^2_{clk} as unknown. Unlike its ionospheric counterpart, the clock process noise variance σ^2_{clk} is not assumed to be the function of the zenith angles $z_j (j = 1, \dots, m)$. This is because there is no evidence of the dependency of σ^2_{clk} on z is observed in our results. To illustrate this, we used the system of observation Eqs. (12) and estimated the ionospheric and clock process noise variances of each individual GPS satellite to identify the stated dependency. The corresponding results over one day have been shown in Fig. 4. The ionospheric variances exponentially increase as the zenith angle z increases. This is, however, not the case with their clock counterparts. Note also that the fixed value of 15°, set as the denominators in (13), has been determined by an application of curve fitting to the ionospheric estimated variances shown in the top panel of Fig. 4. In the next section, we base our analysis on the assumptions made in the dynamic models (13) and (14) and study the time-variability of the stated corrections under various circumstances.

Datasets and ionospheric contributing factors

The values, shown as black dots in Fig. 4, are the estimated process noise variances over one day. Using an application of least-squares estimation, one can combine these values to estimate a daily process noise variance solution for each of the correction types. In this section, we present the square-root of such daily variance estimates, i.e., the STDs of ionospheric and satellite clock process noises $\hat{\sigma}_{\text{iono}}$ and $\hat{\sigma}_{\text{clk}}$, respectively.

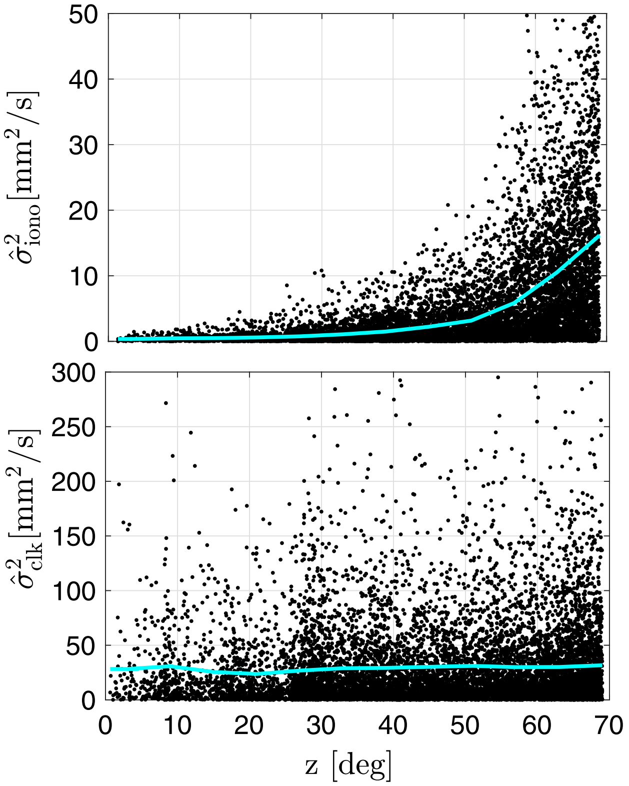

Fig. 4 Estimated values of the ionospheric (top) and clock (bottom) process noise variances of individual GPS satellites based on the zenith angle of the ionospheric piercing point z over 24 h, using station CUT0, on September 1, 2020. The solid cyan lines indicate the corresponding average values at every 5° interval

Data description

The GNSS datasets from eight globally distributed IGS permanent stations, as outlined in Table 2, are utilized in this study. We only use the carrier-phase measurements to avoid code multipath modeling errors. The satellite constellations considered are GPS (L1/L2) and Galileo (E1/E5a) with a 30-s measurement sampling-rate, for which the phase measurement noise of $1\text{mm}/\sin(\text{ele})$ (ele: satellite elevation) is assumed to form the variance matrices $Q_{n_{i-1}}$ and Q_{n_i} in (12), see e.g., de Bakker et al. (2012). The elevation cut-off elevation angle is set to 10°.

Ionospheric process noise STD

To demonstrate the relationship between the estimated ionospheric process noise STD and the solar flux index F10.7, we conducted an analysis using approximately 11 years of CUT0 datasets. Although solar activity dominates during the day, it can influence the ionosphere indirectly at night, e.g., by changing the Earth magnetic field. Therefore, we process data for both daytime and nighttime intervals.

Table 2 Information regarding the globally distributed GNSS permanent stations studied in this study. All stations, except CUT0, PERT, and PALM, are in the Northern Hemisphere. ANMG and PERT are in the proximity of SIN1 and CUT0, respectively

Stations	Country	Lat (°)	Lon (°)	Receiver	Antenna–Radome
SIN1	Singapore	1	103	TRIMBLE NETR9	LEIAR25.R3—LEIT
ANMG	Malaysia	3	102	TRIMBLE NETR9	JAVRINGANT_DM—SCIS
PTGG	Philippines	15	121	SEPT POLARX5	TRM59800.00—SCIS
CUT0	Australia	− 32	116	TRIMBLE NETR9	TRM59800.00—SCIS
PERT	Australia	− 32	116	TRIMBLE ALLOY	TRM59800.00—NONE
ZIM3	Switzerland	47	7	TRIMBLE NETR9	TRM59800.00—NONE
UCAL	Canada	51	− 114	TRIMBLE NETR9	TRM57971.00—NONE
PALM	Antarctica	− 65	− 64	SEPT POLARX5	ASH700936D_M—SCIS

However, we demonstrate this dependence using daytime data. Distinct daytime and nighttime intervals are established by referencing the local time at each station based on sunrise and sunset times. The daytime interval for stations SIN1, ANMG, PTGG, CUT0, and PERT (LT = UTC + 8 h) is chosen as 8 a.m. to 5 p.m., with the nighttime interval as 8 p.m. to 5 a.m. For station ZIM3 (LT = UTC + 1 h/2 h), the daytime interval is chosen as 9 a.m. to 3 p.m., with the nighttime interval as 10 p.m. to 4 a.m. For station UCAL (LT = UTC − 6 h/7 h), the daytime interval is taken as 9 a.m. to 4 p.m., with the nighttime interval as 10 p.m. to 5 a.m. PALM (LT = UTC − 3 h) follows a different pattern every month (e.g., in July, the daytime hours are from 12 p.m. to 3 p.m., due to the short duration of sunlight, and the nighttime hours are from 9 p.m. to 5 a.m.). To observe the impact of multi-constellation, we also performed the same processing using the GPS-plus-Galileo setup from January 2020 to March 2023. This analysis is then repeated for different stations to illustrate the variation of ionospheric process noise STD across different geographic latitudes.

Local time dependency

Figure 5 shows the estimated process noise STD variation as a function of local time at station CUT0 (LT = UTC + 8h) on March 1, 2023 (top panel) and September 1, 2020 (bottom panel). The ionospheric process noise STD exhibits higher values during the daytime and decreases during nighttime hours. On the solar maximum day (March 1, 2023), not only is the variation in ionospheric process noise STD higher, but also the duration of high ionospheric process noise STD during the daytime is extended.

Solar activity dependency

Solar activity, characterized by the 11-year cycle of solar flux index F10.7, has been widely recognized as one of the drivers of ionospheric dynamics (Tapping 1987). One would expect to observe a correlation between the solar flux index F10.7 and the ionospheric process noise STD. We determine the daily solutions $\hat{\sigma}_{\text{iono}}$ per month, computing their monthly error bars at the 95% confidence level. Figure 6 shows the stated monthly error bars for CUT0 during the daytime using GPS data. Additionally, the monthly average solar flux index F10.7 is illustrated by a pink line, shown on the right y-axis of the figure. The temporal variations of the solar flux index F10.7 and ionospheric process noise STD share a noticeable resemblance, indicating a strong correlation between them. Despite their distinct numerical values and units, their signatures remarkably coincide.

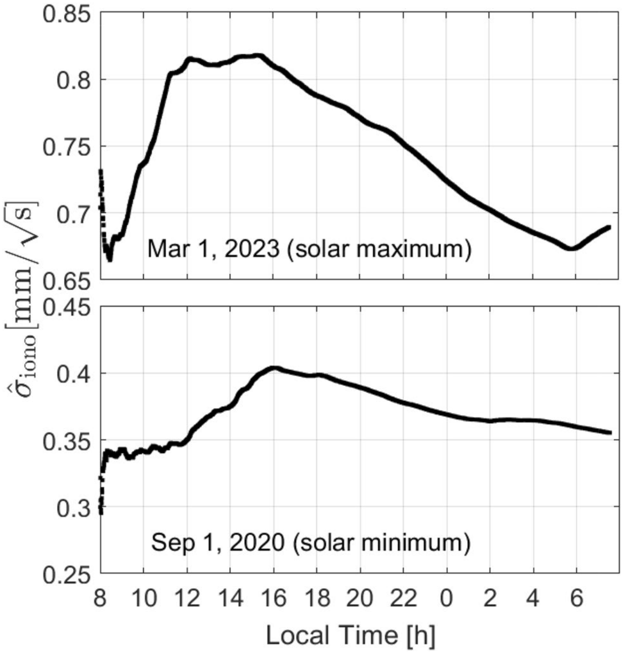

Fig. 5 Diurnal variation of the estimated ionospheric process noise STD for CUT0 using GPS-plus-Galileo on March 1, 2023 (top) and September 1, 2020 (bottom). Solar maximum refers to when the solar activity reaches its peak, while solar minimum refers to the periods with a minimal solar activity

The corresponding error bars during nighttime are shown in Fig. 7. The figure reflects the observation that the ionospheric activities are generally low during the night, resulting in a smaller process noise STD. Significant disparity in daytime and nighttime process noise STDs emerge on solar

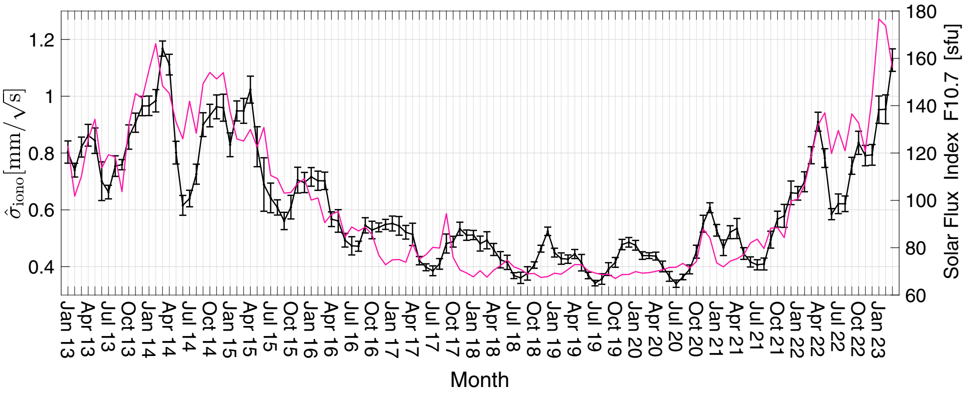

Fig. 6 Estimated monthly error bars of the ionospheric process noise STD (left *y*-axis) for CUT0 using GPS over a span of approximately 11 years. The data are collected during the daytime period. The monthly average solar flux index F10.7 (pink line) is plotted on the right *y*-axis

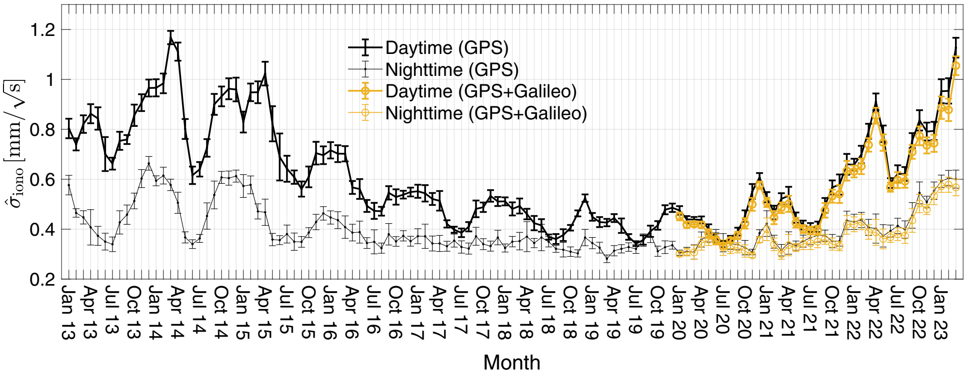

Fig. 7 Estimated monthly error bars of the ionospheric process noise STD for CUT0 during the period of daytime (thick line) and nighttime (thin line). They are derived using GPS from January 2013 to March 2023 (black) and using GPS-plus-Galileo from January 2020 to March 2023 (yellow)

maximum periods. To verify the solutions of the ionospheric process noise $\sigma_{\rm iono}$, the GPS-plus-Galileo data from January 2020 to March 2023 are also processed to re-compute $\hat{\sigma}_{\rm iono}$ and are shown in the same figure (Fig. 7). Both estimated error bars yield almost identical process noise STDs.

Geographic latitude dependency

Figure 8 shows the estimated monthly mean values of the ionospheric process noise STD for the stations in low-latitude (top), mid-latitude (middle), and high-latitude (bottom) regions during daytime (left) and nighttime (right). We first focus on the stations in low-latitude regions, i.e., SIN1 ($\phi = 1°$) and PTGG ($\phi = 15°$). During the daytime, PTGG exhibits a systematically higher process noise STD compared to SIN1. Conversely, during the night, this relationship is reversed, with SIN1 having a higher ionospheric process noise STD than PTGG. In the equatorial region, daytime ionosphere maxima occur on both sides of the geomagnetic equator at a latitude of approximately ±15° (Hernández-Pajares et al. 2011). This phenomenon is referred to as the equatorial fountain, which is reflected in the ionospheric process noise STD. However, during the night, the ionosphere exhibits a maximum near the magnetic equator (Chen et al. 2008), with SIN1 having a higher mean ionospheric process noise STD than PTGG.

Now, consider the stations in mid-latitude regions. CUT0 ($\phi = -32°$), in an early mid-latitude area, typically exhibits higher estimated monthly mean values of the ionospheric process noise STD compared to the mean values of ZIM3 ($\phi = 46°$) and UCAL ($\phi = 51°$), with UCAL having the lowest mean values among them. However, there are irregularities in the mean values for certain months, mainly during solar maximum and nighttime periods. These are due to seasonal variations and geomagnetic activities (Araujo-Pradere et al. 2005).

Finally, we examine the station PALM ($\phi = -64°$) in a high-latitude region. PALM experiences the lowest estimated daytime mean values of ionospheric process noise STDs compared to stations at lower latitudes. Like mid-latitude stations, irregularities arise due to seasonal variations and geomagnetic activities. However, during the nighttime, these factors produce an annual pattern with maximum occurrence during the summer solstice.

Figure 8 presents mean values of the ionospheric process noise STD of the stations, while Fig. 9 shows the corresponding monthly error bars during daytime and nighttime for every station, along with the monthly averaged solar flux index F10.7. Let us first discuss the relationship between the monthly averaged solar flux index F10.7 and daytime monthly error bars of the ionospheric process noise STDs. A noticeable trend is observed, indicating that as the latitude

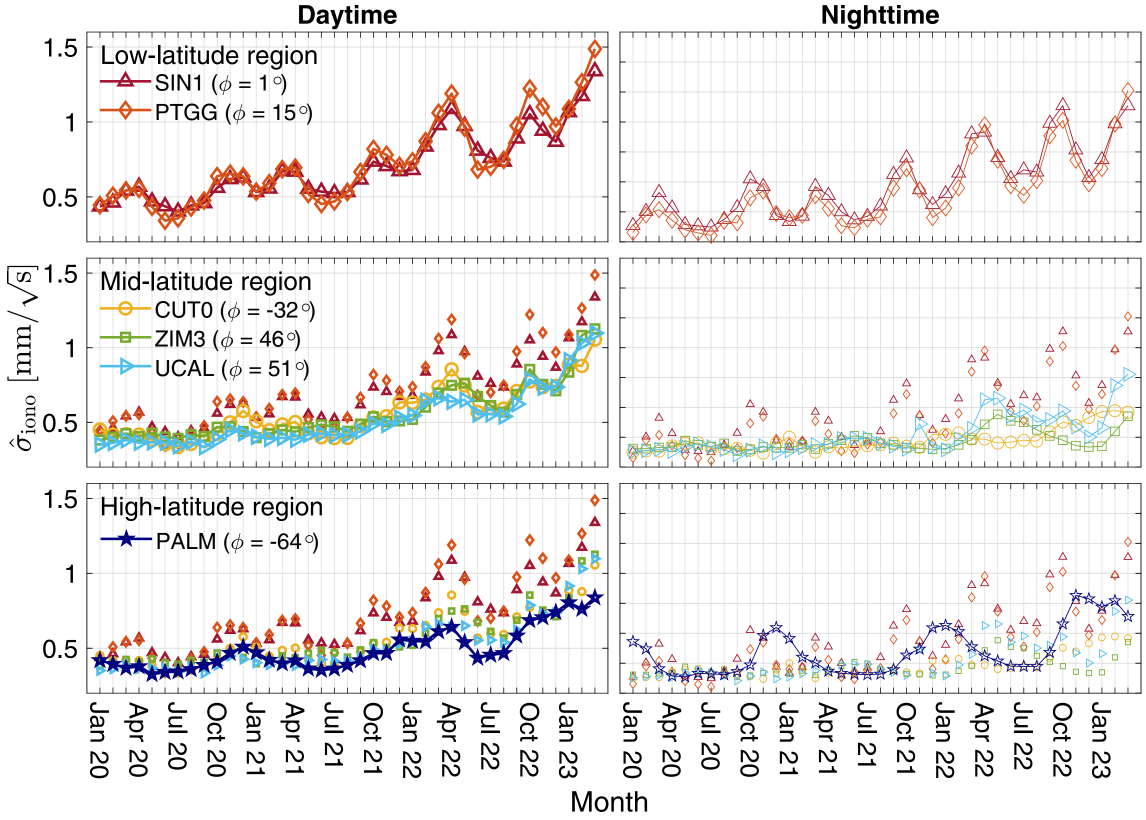

Fig. 8 Estimated monthly mean values of the ionospheric process noise STD for globally distributed GNSS permanent stations, located in low-latitude (top), mid-latitude (middle, including mean values of stations in low-latitude), and high-latitude (bottom, including mean values of stations in low- and mid-latitude) regions, at daytime (left) and nighttime (right) periods, spanning from January 2020 to March 2023 using GPS-plus-Galileo

increases, the alignment between the solar flux index F10.7 and the ionospheric process noise STD diminishes, especially during the solar maximum periods. For instance, process noise STD of PALM shows the least indication of any remaining dependency on solar flux index F10.7. The impact of the solar activity specifically changes in the F10.7 parameter, has a more significant effect on the ionosphere at lower latitudes (Galav et al. 2010), which is reflected in the ionospheric process noise STDs. This is because the ionosphere in these areas receives a higher level of direct sunlight, leading to a greater impact of solar activity on the ionization processes occurring within the ionosphere. As to the magnitude of the ionospheric process noise STD over days and nights, the estimated values remain high during the nighttime in low-latitude regions. As latitude increases, both the daytime and nighttime process noise STDs decrease. However, at PALM, in high-latitude regions, process noise STD shows an abnormal minimum at daytime and maximum at nighttime during the summer solstice. These unusual characteristics can be attributed to the movement of ionization in a horizontal direction, guided by the earth magnetic field (Rastogi 1960).

Seasonal variations

Figure 9 also illustrates the visible seasonal variations at every station. In SIN1 and PTGG, in the Northern Hemisphere, the estimated process noise STDs reveal an annual periodicity in which peaks occur in March or April (spring equinox) and September or October (autumn equinox), while valleys occur during the winter (November, December, January, and February) and the summer (May, Jun, July, and August) solstices. During the summer and winter solstices, the ionosphere is relatively calm overnight, resulting in the lowest levels of process noise STDs, while the discrepancy between nighttime and daytime STDs is larger.

In the case of station CUT0, in the Southern Hemisphere, seasonal variation is not obvious during solar minimum periods. During the solar maximum years (Fig. 7), the process noise STD reaches its peak in March or April (autumn equinox) and decreases to its lowest value in Jun or July (winter solstice). Consider now the two remaining stations in mid-latitude regions, ZIM3 and UCAL, in the Northern Hemisphere. There are two observed peaks annually, one in March (spring equinox) and the other in October (autumn

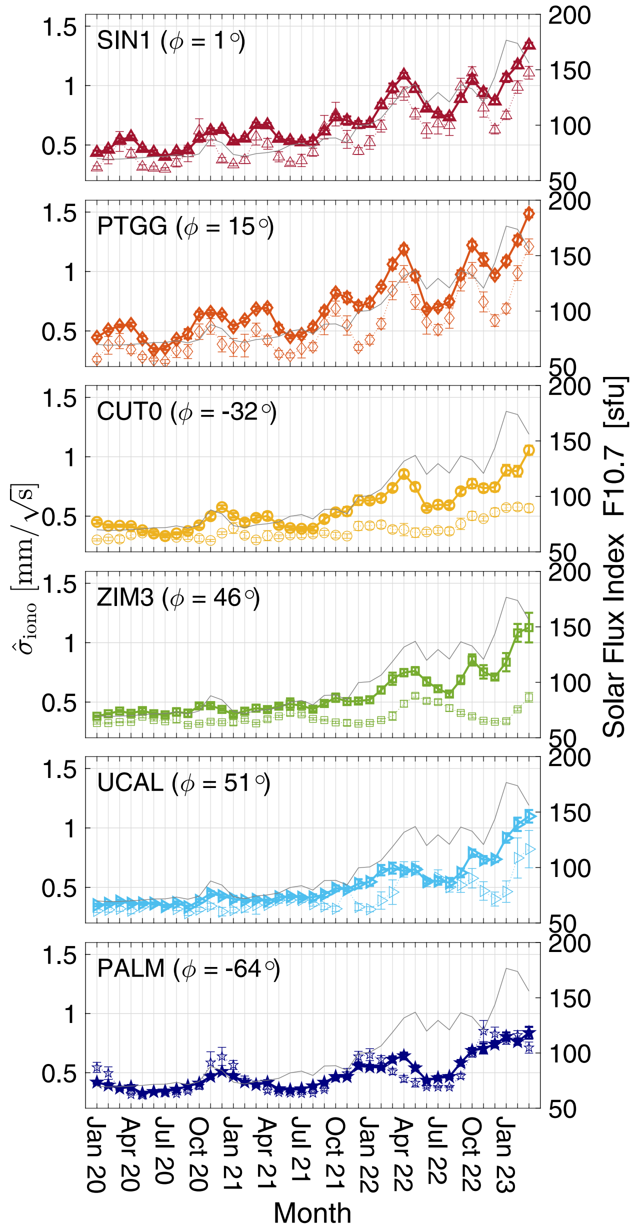

Fig. 9 Monthly error bars of the ionospheric process noise STD for globally distributed GNSS permanent stations during daytime (thick lines) and nighttime (thin lines) spanning from January 2020 to March 2023 using GPS-plus-Galileo. CUT0 and PALM are in the Southern Hemisphere, while the remaining stations are in the Northern Hemisphere. The monthly average solar flux index F10.7 (gray line) is plotted on the right *y*-axis for every station

equinox). It tends to increase during the winter solstice and equinoxes but remains relatively stable during the summer solstice (May, Jun, July, and August), reflecting the ionospheric variability pattern (Araujo-Pradere et al. 2005).

Regarding PALM, in the Southern Hemisphere, there are also two peaks in the estimated ionospheric process noise STDs during daytime. The largest peak occurs in December (summer solstice), while the secondary peak occurs in April (autumn equinox). During nighttime, there is an annual pattern with a maximum during the summer solstice (November, December, January, and February) and a minimum during the winter solstice (May, Jun, July, and August), which aligns with the annual variations of the solar zenith angle (Ratovsky et al. 2014).

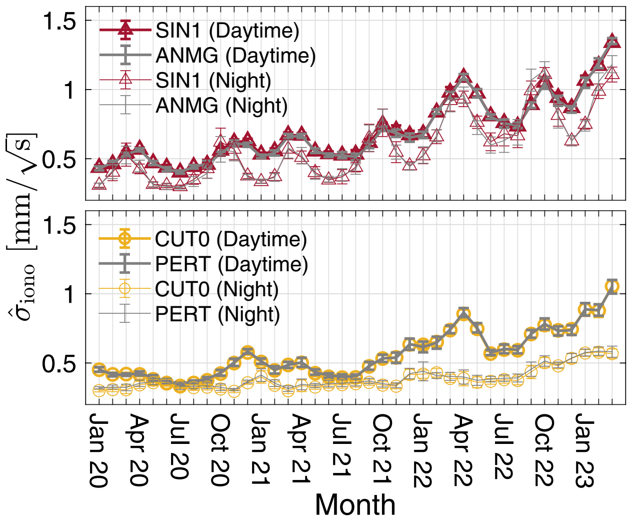

Fig. 10 Monthly error bars of the ionospheric process noise STD for two station pairs, SIN1 and ANMG (top), and CUT0 and PERT (bottom) during the period of daytime (thick line) and nighttime (thin line) spanning from January 2020 to March 2023 using GPS-plus-Galileo. The inter-station distance between SIN1 and ANMG is approximately 300 km, while the distance between CUT0 and PERT is approximately 20 km

We also investigate the behavior of the ionospheric process noise for nearby stations, see Fig. 10. The corresponding nearly identical error bars imply that if the ionospheric process noise STD is estimated by a provider, nearby users can utilize the same value to construct the variance matrix of their corrected observations.

Satellite clock process noise STD

In this section, we discuss how the estimation of the satellite clock process noise σ_{clk} can be adversely affected by satellite orbital biases using two pairs of GNSS stations that are located at a considerable distance from one another. The daily estimated process noise STD for the satellite clock at CUT0 and UCAL throughout the year 2022 (day-of-year, DoY) is presented in Fig. 11. The estimation is carried out based on precise and navigation satellite orbit products, focusing on the Galileo and GPS Block3 satellites. Recall from (7) that these estimated STDs are driven by the measurements $y_i - A_i x_i$, thus being dependent on the a priori values x_i. This means that any modeling errors, such as orbital biases and incorrectly assigned ground-truth station

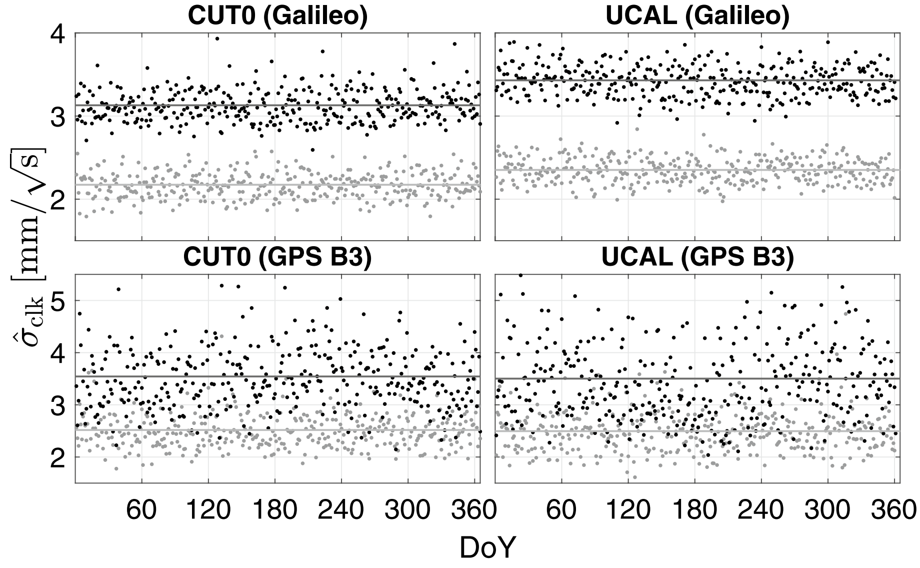

Fig. 11 The daily estimated satellite clock process noise STD for CUT0 (left) and UCAL (right) using satellites of Galileo (top) and GPS block3 (bottom) over the entire DoY of 2022. The obtained results are presented separately for two types of orbits, precise (gray) and navigation (black) with their corresponding average values

coordinates, can affect the process noise variance estimates. This has been reflected in Fig. 11. The satellite clock process noise is over-estimated when one uses the navigation orbits (black dots). This is due to the biases present in the navigation orbits. By using the precise orbit products (gray dots), one obtains satellite clock process noise estimated values that are smaller. Ideally, the solutions of the satellite clock process noise must be independent of the location of the receiver. Figure 11 indicates small deviations between the estimated clock process noise of two stations CUT0 and UCAL.

Figure 11 also indicates that the estimated process noise STD for the Galileo satellite clocks is smaller than that of their GPS block3 counterparts. This corroborates that the Galileo system exhibits a higher proportion of satellites with reduced clock noise when compared to GPS, which is attributed to the utilization of highly accurate passive hydrogen maser clocks within the majority of the Galileo constellation (Carlin et al. 2021).

Impact of the uncertainty of the estimated process noises

Earlier, we showed that the user IAR performance can be deteriorated if the nominal values of the process noise of the corrections would be too different from their true versions (Fig. 3). It is then proposed to directly determine the process noises σ_{iono} and σ_{clk} from GNSS data. However, the numerical results presented in this section indicate that estimated values of these process noises can be accompanied by an amount of uncertainty. For instance, the monthly solutions of the ionospheric process noise σ_{iono} exhibit the 95% confidence intervals $[\hat{\sigma}_{\mathrm{iono}} - \Delta_{\mathrm{iono}}, \hat{\sigma}_{\mathrm{iono}} + \Delta_{\mathrm{iono}}]$ with the positive scalar $\Delta_{\mathrm{iono}} \approx 0.05\ \mathrm{mm}/\sqrt{\mathrm{s}}$ (Fig. 7). Likewise, Fig. 11 indicates that the daily solutions of the satellite clock process noise σ_{clk} can have confidence intervals $[\hat{\sigma}_{\mathrm{clk}} - \Delta_{\mathrm{clk}}, \hat{\sigma}_{\mathrm{clk}} + \Delta_{\mathrm{clk}}]$ with the positive scalar $\Delta_{\mathrm{clk}} \approx 0.5\ \mathrm{mm}/\sqrt{\mathrm{s}}$, where $\Delta = 2\sigma$.

To address how the user IAR performance is affected if one chooses a value within such confidence intervals, we conduct a sensitivity analysis. The results are summarized in Tables 3 and 4 for a latency of $\tau = 10$ seconds. Table 3

Table 3 User single-epoch ambiguity success rates when the true (σ_{clk}) and estimated ($\hat{\sigma}_{\mathrm{clk}}$) value of the satellite clock process noise are fixed to $\sigma_{\mathrm{clk}} = \hat{\sigma}_{\mathrm{clk}} = 7\ \mathrm{mm}/\sqrt{\mathrm{s}}$, whereas the estimated value of ionospheric process noise takes the values $\hat{\sigma}_{\mathrm{iono}} = \sigma_{\mathrm{iono}} \pm q\Delta_{\mathrm{iono}} (q = 1, \ldots, 4)$ with $\sigma_{\mathrm{iono}} = 0.4\ \mathrm{mm}/\sqrt{\mathrm{s}}$ and $\Delta_{\mathrm{iono}} = 0.05\ \mathrm{mm}/\sqrt{\mathrm{s}}$. This analysis corresponds to the data presented in Table 1 for latency of $\tau = 10$ seconds

Systems	Ambiguity success rate (%)				
	σ_{iono}	$\sigma_{\mathrm{iono}} \pm \Delta_{\mathrm{iono}}$	$\sigma_{\mathrm{iono}} \pm 2\Delta_{\mathrm{iono}}$	$\sigma_{\mathrm{iono}} \pm 3\Delta_{\mathrm{iono}}$	$\sigma_{\mathrm{iono}} \pm 4\Delta_{\mathrm{iono}}$
GPS	98.7	98.7, 98.7	98.5, 98.6	98.2, 98.4	97.7, 98.3
GPS + Galileo	99.4	99.4, 99.4	99.3, 99.3	99.3, 99.3	99.2, 99.3

Table 4 User single-epoch ambiguity success rates when the true (σ_{iono}) and estimated ($\hat{\sigma}_{\text{iono}}$) value of the ionospheric process noise are fixed to $\sigma_{\text{iono}} = \hat{\sigma}_{\text{iono}} = 0.4\ \text{mm}/\sqrt{\text{s}}$,, whereas the estimated value of satellite clock process noise takes the values $\hat{\sigma}_{\text{clk}} = \sigma_{\text{clk}} \pm q\Delta_{\text{clk}}(q = 1, \ldots, 4)$ with $\sigma_{\text{clk}} = 7\ \text{mm}/\sqrt{\text{s}}$ and $\Delta_{\text{clk}} = 0.5\ \text{mm}/\sqrt{\text{s}}$. This analysis corresponds to the data presented in Table 1 for latency of $\tau = 10$ seconds

Systems	Ambiguity success rate (%)				
	σ_{clk}	$\sigma_{\text{clk}} \pm \Delta_{\text{clk}}$	$\sigma_{\text{clk}} \pm 2\Delta_{\text{clk}}$	$\sigma_{\text{clk}} \pm 3\Delta_{\text{clk}}$	$\sigma_{\text{clk}} \pm 4\Delta_{\text{clk}}$
GPS	98.7	98.7, 98.7	98.6, 98.6	98.4, 98.6	98.2, 98.5
GPS + Galileo	99.4	99.4, 99.4	99.3, 99.3	99.3, 99.3	99.2, 99.2

presents the user single-epoch ambiguity success rates when the true and estimated value of the satellite clock process noise are fixed to $\sigma_{\text{clk}} = \hat{\sigma}_{\text{clk}} = 7\ \text{mm}/\sqrt{\text{s}}$, whereas the estimated value of ionospheric process noise takes the values $\hat{\sigma}_{\text{iono}} = \sigma_{\text{iono}} \pm q\Delta_{\text{iono}}(q = 1, \ldots, 4)$ with $\sigma_{\text{iono}} = 0.4\ \text{mm}/\sqrt{\text{s}}$. Similarly, Table 4 considers the case where the true and estimated value of the ionospheric process noise are fixed to $\sigma_{\text{iono}} = \hat{\sigma}_{\text{iono}} = 0.4\ \text{mm}/\sqrt{\text{s}}$, whereas the estimated value of satellite clock process noise takes the values $\hat{\sigma}_{\text{clk}} = \sigma_{\text{clk}} \pm q\Delta_{\text{clk}}$ with $\sigma_{\text{clk}} = 7\ \text{mm}/\sqrt{\text{s}}$. Both the GPS and GPS-plus-Galileo cases are considered. The comparison of the first two columns in both tables shows that no significant drop in the user ambiguity success rate is experienced when one adopts the nominal values $\sigma_{\text{iono}} \pm \Delta_{\text{iono}}$ and $\sigma_{\text{clk}} \pm \Delta_{\text{clk}}$. However, when one chooses nominal values that are further away from the stated confidence intervals (i.e., when $q \geq 2$, which corresponds to intervals larger than 4σ confidence interval), the ambiguity success rate becomes lower than its optimal value.

Concluding remarks

In this contribution, we presented an estimation method to determine the process noise variance of PPP-RTK corrections using single-receiver GNSS data. The importance of using such data-driven variance estimates stems from the fact that the estimation method of the user needs to account for the uncertainty of the time-predicted corrections. Otherwise, the parameter solutions experience a considerable precision loss, deteriorating the IAR performance. While the proposed variance estimation method can be applied to any type of PPP-RTK corrections, here, particular attention was given to the process noise estimation of the ionospheric delays. It illustrated how the ionospheric process noise responds to the ionospheric time-variability, being a function of the solar activity, local time, and the geographic latitude of the receiver. We highlighted, in the presence of orbital and station coordinate biases, that the solutions of the satellite clock process noise can be over-estimated. Our main findings are summarized as follows:

- Unlike the user single-epoch float positioning solutions, the corresponding fixed solutions can experience a significant precision loss when the process noise of the corrections is incorrectly specified. When the correction latency exceeds 5 s, the user estimation methods fail to correctly report the precision description of both the float and fixed solutions.
- The close resemblance between the estimated ionospheric process noise and the solar flux index F10.7 over 11 years indicates a strong correlation between these two quantities, suggesting that ionospheric process noise estimates can also be employed to sense the ionospheric time-variability.
- The statistically significant difference between the ionospheric process noise estimates during daytime and nighttime indicates that both the provider and user should equip their Kalman filters with time-dependent ionospheric process noises.
- By studying the dependency of the ionospheric process noise estimates on the geographic latitude of the receiver, a decline in the magnitude of the ionospheric process noise is observed the larger the latitude becomes.
- The estimated error bars of the ionospheric process noise were shown to be almost identical for nearby stations. This implies that if a provider estimates the ionospheric process noise, nearby users can utilize the same value to construct the variance matrix of their corrected observations.

Acknowledgements The GNSS data/products are made available by the International GNSS Service (IGS) and Geoscience Australia. The solar flux index F10.7 data is supplied by the GSFC/SPDF OMNIWeb interface. All this support is gratefully acknowledged.

Author contributions PSN and AK initiated the concept and the framework. PSN conducted the analysis and wrote the main manuscript text. All the authors reviewed and edited the manuscript.

Data availability The GNSS data are accessible from https://cddis.nasa.gov/archive/gnss/data/ and https://data.gnss.ga.gov.au/. Likewise, the orbit products are accessible through https://cddis.nasa.gov/archive/gnss/products/mgex/. The solar flux index F10.7 data are available at https://omniweb.gsfc.nasa.gov.

Declarations

Conflict of interests The authors declare no competing interests.

Consent to participate Not applicable.

Consent for publication Not applicable.

Ethics approval Not applicable.

References

Adebiyi S, Adimula I, Oladipo O (2014) Seasonal variations of GPS derived TEC at three different latitudes of the southern hemisphere during geomagnetic storms. Adv Space Res 53(8):1246–1254

Amiri-Simkooei A (2007) Least-squares variance component estimation: theory and GPS applications. Dissertation, Delft University of Technology

Amiri-Simkooei A, Tiberius C (2007) Assessing receiver noise using GPS short baseline time series. GPS Solut 11:21–35

Araujo-Pradere E, Fuller-Rowell T, Codrescu M, Bilitza D (2005) Characteristics of the ionospheric variability as a function of season, latitude, local time, and geomagnetic activity. Radio Sci 40(05):1–15

Carlin L, Hauschild A, Montenbruck O (2021) Precise point positioning with GPS and Galileo broadcast ephemerides. GPS Solut 25(2):77

Chen Y, Liu L, Le H (2008) Solar activity variations of nighttime ionospheric peak electron density. J Geophys Res 113(A11).

Collins P, Lahaye F, Bisnath S (2012) External ionospheric constraints for improved PPP-AR initialisation and a generalised local augmentation concept. In: Proceedings of ION GNSS 2012, Institute of Navigation, Tennessee, USA. 17–21 September, pp 3055–3065

de Bakker P, Tiberius C, Van Der Marel H, van Bree R (2012) Short and zero baseline analysis of GPS L1 C/A, L5Q, GIOVE E1B, and E5aQ signals. GPS Solut 16:53–64

Galav P, Dashora N, Sharma S, Pandey R (2010) Characterization of low latitude GPS-TEC during very low solar activity phase. J Atmos Sol-Terr Phys 72(17):1309–1317

Hernández-Pajares M, Juan JM, Sanz J, Aragón-Àngel À, García-Rigo A, Salazar D, Escudero M (2011) The ionosphere: effects, GPS modeling and the benefits for space geodetic techniques. J Geod 85:887–907

Khodabandeh A (2021) Single-station PPP-RTK: correction latency and ambiguity resolution performance. J Geod 95(4):42

Khodabandeh A, Teunissen P, Psychas D (2023) On the problem of double-filtering in PPP-RTK. Sensors 23(1):229

King J, Papitashvili N (2005) Solar wind spatial scales in and comparisons of hourly Wind and ACE plasma and magnetic field data. J Geophys Res 110(A2).

Leick A, Rapoport L, Tatarnikov D (2015) GPS satellite surveying. Wiley, Hoboken

Odijk D, Zhang B, Khodabandeh A, Odolinski R, Teunissen P (2016) On the estimability of parameters in undifferenced, uncombined GNSS network and PPP-RTK user models by means of S-system theory. J Geod 90(1):15–44

Psychas D, Khodabandeh A, Teunissen P (2022) Impact and mitigation of neglecting PPP-RTK correctional uncertainty. GPS Solut 26(1):33

Rastogi R (1960) Abnormal features of the F2 region of the ionosphere at some southern high-latitude stations. J Geophys Res 65(2):585–592

Ratovsky KG, Shi JK, Oinats AV, Romanova EB (2014) Comparative study of high-latitude, mid-latitude and low-latitude ionosphere on basis of local empirical models. Adv Space Res 54(3):509–516

Tapping K (1987) Recent solar radio astronomy at centimeter wavelengths: The temporal variability of the 10.7-cm flux. J Geophys Res 92(1):829–838

Teunissen P, de Bakker P (2013) Single-receiver single-channel multi-frequency GNSS integrity: outliers, slips, and ionospheric disturbances. J Geod 87:161–177

Teunissen P (2000) Adjustment theory: an introduction. Delf University Press, Delft

Teunissen P, Amiri-Simkooei A (2008) Least-Squares Variance Component Estimation. J Geod 82:65–82

Wübbena G, Schmitz M, Bagge A (2005) PPP-RTK: precise point positioning using state-space representation in RTK networks. In: Proceedings of ION GNSS 2005, Institute of Navigation, Long Beach, CA, USA, pp 2584–2594

Wang K, Khodabandeh A, Teunissen P (2017) A study on predicting network corrections in PPP-RTK processing. Adv Space Res 60(7):1463–1477

Zha J, Zhang B, Liu T, Hou P (2021) Ionosphere-weighted undifferenced and uncombined PPP-RTK: theoretical models and experimental results. GPS Solut 25(4):135

Zhang B, Teunissen P, Yuan Y (2017) On the short-term temporal variations of GNSS receiver differential phase biases. J Geod 91:563–572

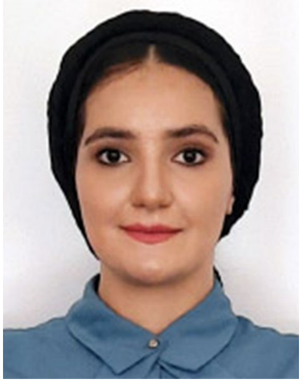

Parvaneh Sadegh Nojehdeh is a Ph.D. candidate at the University of Melbourne. Her research focuses on modeling the ionosphere to obtain precise point positioning with integer ambiguity resolution.

Amir Khodabandeh is a Senior Lecturer at the Department of Infrastructure Engineering at the University of Melbourne. His research interests include estimation theory, interferometric positioning, and GNSS quality control.

Kourosh Khoshelham is an Associate Professor at the University of Melbourne, Melbourne, Australia. His research interests include positioning, 3D mapping and modeling, automated imagery, and point cloud interpretation.

Alireza Amiri-Simkooei is an Assistant Professor at the Department of Geoscience and Remote Sensing, Delft University of Technology. His research interests include optimization and estimation theory and stochastic modeling and processes.